



## Revealing the key oxidative species generated by Pt-loaded metal oxides under dark and light conditions

Wibawa H. Saputera, Jason A. Scott\*, Donia Friedmann, Rose Amal\*

Particles and Catalysis Research Group, School of Chemical Engineering, Faculty of Engineering, University of New South Wales, Australia



### ARTICLE INFO

**Keywords:**

Reactive oxygen species (ROS)  
Surface active oxygen  
Low temperature dark catalysis  
Light pre-treatment  
Photocatalysis  
Platinum  
Metal oxides  
Formic acid

### ABSTRACT

The role of key oxidative species in formic acid oxidation using neat and platinum-loaded  $\text{TiO}_2$ ,  $\text{CeO}_2$  and  $\text{SiO}_2$  was investigated. The catalytic reactions under three different illumination conditions; dark catalysis (i.e. no illumination), dark catalysis with UV light pre-treatment (denoted as pre-30) and photocatalysis (i.e. continuous UV illumination), were studied. The activities of neat  $\text{TiO}_2$ ,  $\text{CeO}_2$  and  $\text{SiO}_2$  were low under dark and pre-30 conditions while under illumination (photocatalysis) the semiconductor metal oxides,  $\text{TiO}_2$  and  $\text{CeO}_2$  showed much higher oxidation rates. For the Pt-loaded catalysts, the key active species were surface active oxygen ( $\text{PtO}_{\text{ads}}$  and  $\text{O}_{\text{ads}}^-$ ) under the dark catalytic condition with and without light pre-treatment while under photocatalytic condition, photogenerated holes and electrons are believed to form hydroxyl radicals ( $\cdot\text{OH}$ ) and superoxide radicals ( $\cdot\text{O}_2^-$ ), respectively, for  $\text{CeO}_2$ ,  $\text{TiO}_2$ ,  $\text{Pt/TiO}_2$  and  $\text{Pt/CeO}_2$ . Unexpectedly,  $\text{Pt/SiO}_2$  showed the highest activity under the dark catalytic condition. The cuboctahedral shape of the Pt deposits on the  $\text{SiO}_2$  surface, which promote a greater number of sharp edges/corners at the interface, is believed to have been advantageous for dissociating and activating adsorbed oxygen species compared to the Pt deposits on  $\text{TiO}_2$  and  $\text{CeO}_2$ . The Pt deposit shape is thought to be responsible for the observed high activity of  $\text{Pt/SiO}_2$  for the dark catalytic oxidation of formic acid.

### 1. Introduction

Technologies based on catalytic oxidation have been acknowledged as the most effective for environmental pollution control, in particular for the abatement of volatile organic compounds (VOCs). Catalytic oxidation has shown potential as being environmentally friendly, non-toxic, versatile, and of low-cost. It involves the total oxidation of organic compounds to convert them into harmless products,  $\text{CO}_2$  and  $\text{H}_2\text{O}$ , under ambient conditions [1–3]. Noble metal catalysts such as Pt [1,2], Au [3], Pd [4], and Ag [5] have been used for the catalytic oxidation of VOCs under ambient conditions. Among these catalysts, Pt-based catalysts, despite their cost, have been the subject of great interest for eliminating VOCs due to their high activity, stability and ability to be regenerated [1,2,6]. One of the attractive features of Pt-based catalysts is the ability of Pt to scavenge photogenerated electrons upon UV-illumination [7] and reduce charge carrier recombination [7,8]. Pre-treating  $\text{Pt/TiO}_2$  catalysts with UV light might also enhance its activity by increasing the amount of active species, or favorably changing their nature for the degradation of organic pollutants. Denny et al. [9] reported that the dark, low temperature catalytic oxidation of formic acid after light pre-treatment of  $\text{Pt/TiO}_2$  catalysts showed

comparable oxidation rates to the photocatalytic case. Recently, our group reported that the light pre-treatment of  $\text{Pt/TiO}_2$  enhanced formic acid oxidation by seven-fold in aqueous systems when compared with the untreated catalyst [10].

The enhancement of activity after UV pre-illumination treatment of the catalyst, prior to the dark catalytic oxidation reaction has been explained as arising from an enhancement of the dissociation and activation of oxygen molecules [9,10]. From a photocatalytic perspective, there have been many studies on the mechanism of organic pollutant degradation using supported Pt photocatalysts. Typically, such studies have discussed the organic oxidation occurring via reactive oxygen species (ROS) generation upon irradiation with UV-light. ROS are chemically reactive molecules containing oxygen such as hydroxyl radicals ( $\cdot\text{OH}$ ), singlet oxygen ( ${}^1\text{O}_2$ ), hydrogen peroxide ( $\text{H}_2\text{O}_2$ ) and superoxide radicals ( $\cdot\text{O}_2^-$ ). From other photocatalysis studies, it is known that metal oxide-supported Pt deposits can produce the superoxide anion radical and the hydroxyl radical. The ability of Pt catalysts to mediate and promote the generation of ROS is of fundamental importance for understanding the mechanism of organic pollutant degradation using supported Pt catalysts and photocatalysts.

The ability of Pt to activate oxygen and promote ROS generation is

\* Corresponding authors.

E-mail addresses: [jason.scott@unsw.edu.au](mailto:jason.scott@unsw.edu.au) (J.A. Scott), [r.amal@unsw.edu.au](mailto:r.amal@unsw.edu.au) (R. Amal).

dependent on a number of factors. These factors include the size [11–13], shape [14–17], and exposed crystal facets of the Pt deposits [18,19] as well as the Pt oxidation state [20–23]. Regarding the Pt deposit shape, various methods have been developed to produce Pt deposits with different shapes, such as hexagonal [14], cuboctahedral [24,25], spheres [26], tubes [27], rods [28], tetrahedral [29], and cubes [30] for diverse applications. For instances, Sanchez et al. [14] reported that the rate of the oxygen reduction reaction (ORR) using different shape-controlled Pt nanoparticles decreased in the order of  $\text{Pt}_{\text{hexagonal}} > \text{Pt}_{\text{tetrahedral}} > \text{Pt}_{\text{spherical}} > \text{Pt}_{\text{cubic}}$ . Li et al. [12] reported that a higher catalytic activity of glycerol oxidation was observed for cuboctahedral Pt compared to tetrahedral Pt. Kovacs et al. [31] studied the effect of Pt shape on hydrogen production using  $\text{Pt}/\text{TiO}_2$  catalyst by comparing spherical and polyhedral Pt. They found the spherical Pt shape was more active with the better activity attributed to more efficient electron transfer due to its high-index crystal facets. The catalytic performance of Pt based catalysts has also been found to be influenced by crystal facets exposed, that is, the surface atomic arrangement. The impact of  $\text{Pt}(111)$ ,  $\text{Pt}(100)$  and  $\text{Pt}(110)$  crystal facets on catalyst performance has been extensively studied [19] and depends on the substrate [32] and catalyst support [33,34]. For instance, Octahedral Pt nanoparticles bound by the (111) facet were found to be more active than cubic Pt bound by the (100) facet for both the ORR [35] and the dehydrocyclization of *n*-heptane [36]. In contrast, cubic Pt particles with exposed Pt (100) facets were found to be more active than octahedral Pt with Pt (111) facets for glycerol oxidation [11], isobutene isomerization [37], and formic acid electrooxidation [16]. The exposed facet influences the binding of the substrates onto the surface and the resulting associated bond strengths, hence affecting reactivity, selectivity and long term catalyst stability [20,38].

The Pt oxidation state has also been found to govern the activities of supported Pt catalysts, with a change in the Pt species having been observed during the catalytic oxidation of different organic pollutants [21–23]. Pt may exist as metallic Pt (denoted as  $\text{Pt}^0$ ) and oxidized Pt (denoted as  $\text{Pt}_{\text{ox}}$  and comprising  $\text{Pt}^{2+}$  and  $\text{Pt}^{4+}$ ).  $\text{Pt}^0$  has generally been reported as the most active oxidation state while  $\text{Pt}_{\text{ox}}$  has been suggested as detrimental to activity by acting as photogenerated electron and hole recombination centers in photocatalytic systems [21]. Additionally, atomic oxygen adsorbed on Pt surface ( $\text{PtO}_{\text{ads}}$ ) resulted from the molecular oxygen dissociation process has been reported to be crucial for oxidizing organic compounds without the presence of UV-light [39–41].  $\text{Pt}^0/\text{TiO}_2$  was found to be more active than  $\text{Pt}_{\text{ox}}/\text{TiO}_2$  for photocatalytically oxidizing 4-chlorophenol, chloroform [21], and acetaldehyde [23]. In the instance of a mixed  $\text{Pt}/\text{TiO}_2\text{-CeO}_2$  catalyst, Rocha, et al. [42] reported an optimal relative proportion of  $\text{Pt}^{2+}$  (~45%) and  $\text{Ce}^{4+}$  species (~30%) for enhancing the catalytic efficiency of phenol oxidation, by providing a high oxygen storage capacity.

When used as a catalyst or photocatalyst, Pt is typically deposited on the surface of a support, for example on the surface of a metal oxide. In this study, we report on our investigation into the key active species formed on Pt deposits (whether metallic or in an oxide form) loaded on  $\text{TiO}_2$ ,  $\text{CeO}_2$  and  $\text{SiO}_2$  supports, using aqueous-phase formic acid oxidation as the probe reaction. Three catalytic systems were considered; dark catalysis (i.e. no illumination), dark catalysis with a UV pre-illumination pre-treatment step (denoted as pre-30) and photocatalysis (i.e. continuous UV illumination). The impact of Pt oxidation state and generated surface active oxygen species on catalyst performance are examined. Effects due to differences in exposed Pt crystal facets, and the size and shape of the Pt deposits are also discussed.

## 2. Experimental

### 2.1. Materials

Aeroxide<sup>®</sup>  $\text{TiO}_2$  P25 (particle size ~25 to 30 nm, surface area

~50  $\text{m}^2 \text{ g}^{-1}$ , anatase to rutile ratio of 4:1 [43]),  $\text{CeO}_2$  (Sigma–Aldrich<sup>®</sup>, particle size < 25 nm) and  $\text{SiO}_2$  (Sigma–Aldrich<sup>®</sup>, particle size ~1–5  $\mu\text{m}$ ) were used as the catalyst supports in all experiments. Chemicals were analytical grade and used as supplied: formic acid (> 98%, Riedel–de Haën), hexachloroplatinic acid (99%, Sigma–Aldrich<sup>®</sup>), perchloric acid (70%, Frederick Chemical), nitrotetrazolium blue chloride (98%, Sigma–Aldrich<sup>®</sup>), and coumarin (98%, Sigma–Aldrich<sup>®</sup>).

### 2.2. Catalyst preparation

All the Pt-based catalysts reported here were prepared via wet impregnation using  $\text{H}_2\text{PtCl}_6$  as the precursor. In a typical synthesis procedure, 2 g of the metal oxide support was dispersed in 200 ml of Milli-Q water.  $\text{H}_2\text{PtCl}_6$  was added drop-wise to the suspension over 30 min to produce a nominal 1 at% Pt loading. The slurry was then dried at 110 °C for 12 h before calcining and hydrogenation in a tube furnace (Labec horizontal tube furnace). Calcination was performed at 300 °C under flowing air with heating and flow rates of 5 °C/min and 50 ml/min, respectively. The calcination condition was maintained for 30 min. Hydrogenation was carried out at 500 °C under a 10 vol%  $\text{H}_2/\text{N}_2$  flowing gas mix with heating and total flow rates of 5 °C/min and 50 ml/min, respectively. The hydrogenation conditions were maintained for 3 h. Three samples comprising neat  $\text{TiO}_2$ ,  $\text{CeO}_2$  and  $\text{SiO}_2$ , were used as controls.

### 2.3. Catalyst characterization

High angle annular dark field scanning transmission electron microscopy (HAADF HR-STEM) and element mapping of the Pt catalysts were performed on a JEOL JEM-ARM200F instrument operating at 200 kV. Particle sizing was conducted using high resolution transmission electron microscopy (HR-TEM) on a Philips CM200 operated at 200 kV and equipped with an energy dispersive x-ray spectroscopy system and SIS CCD camera for digital imaging.

The crystal structure of the samples was determined in air via X-ray diffraction (XRD) using a PANalytical expert multipurpose x-ray diffraction system (MPD) instrument. Data was collected by varying 2 &  $\Theta$ : between 35° and 50° with a step size of 0.026°.

Hydrogen temperature programmed reduction ( $\text{H}_2\text{-TPR}$ ) measurements were recorded using an Autochem II 2920 (Micromeritics) instrument to study the reducibility of the catalyst samples. In a typical measurement, approximately 50 mg of sample was placed into a U-shaped quartz sample tube and heated to 150 °C under 20 ml/min Ar gas (Coregas argon, > 99.99%) at a heating rate of 10 °C/min where it was held for 30 min. Following pre-treatment, the sample was cooled to 50 °C under 20 ml/min Ar. The TPR analysis was conducted under a 10%  $\text{H}_2\text{-Ar}$  (20 ml/min) flow with the temperature ramped from 50 °C to 600 °C at 10 °C/min.

UV-vis spectra were measured with a Shimadzu UV-3600 UV-vis-NIR spectrophotometer using  $\text{BaSO}_4$  as the reference. The total metal content in the catalyst was analyzed using a PerkinElmer OPTIMA 7300 inductively coupled plasma atomic emission spectrometer (ICP-AES), using aqua regia as the digestive agent.

X-ray photoelectron spectroscopy (XPS) analyses were performed using a Thermo ESCALAB250i. The radiation was provided by a monochromatic X-Ray source ( $\text{AlK}\alpha$ , 1486.68 eV) operated at a 164W emission power.  $\text{Ti}2\text{p}$ ,  $\text{Pt}4\text{f}$  and  $\text{O}1\text{s}$  core-level spectra were recorded and the corresponding binding energies were referenced to the  $\text{C}1\text{s}$  peak at 285 eV (from surface carbon). The core-level spectra were deconvoluted into their components with a mixed line shape of Lorentzian (20%) – Gaussian (80%), using the software package Thermo Avantage after subtraction of the Shirley-type background.

### 2.4. Catalytic activity test

The catalytic oxidation of formic acid was assessed using a spiral

reactor as described elsewhere [44]. In a typical measurement, 50 mg of catalyst was loaded into a beaker containing 50 ml of Milli-Q water and then ultra-sonicated for approximately 15 min. The suspension was introduced to the reactor after the pH was adjusted to approximately  $3 \pm 0.05$  using 0.05 M perchloric acid. Light pre-treatment of the catalyst was carried out using UV-light (NEC, 20 W black-light-blue lamp, maximum emission at 365 nm). During light pre-treatment, the suspension was first illuminated for 30 min under an aerobic atmosphere after which the lamp was turned off. The reactor was then opened to the atmosphere and the catalyst suspension circulated for 10 min for air equilibration purposes. The reactor was then sealed and the catalyst suspension circulated for a further 10 min prior to formic acid injection with this period referred to as the ‘relaxation time’. The reaction under continuous illumination (photocatalysis) followed the same procedure described above while keeping the UV light on during the air-equilibration and relaxation steps as well as during the formic acid oxidation process. The reaction under dark conditions (no light pre-treatment) followed the same procedure described above with the exception of there being no UV-light illumination at any stage of the experiment. During formic acid oxidation,  $\text{CO}_2$  generated from the formic acid oxidation process was monitored by a conductivity meter (Jenway 3540). Spent catalysts prior to and following formic acid oxidation were recovered by centrifuging the slurry at 10000 rpm for 30 min. Afterwards, the recovered catalysts were vacuum-dried for 12 h at room temperature in preparation for characterization.

### 2.5. Hydroxyl radical ( $\cdot\text{OH}$ ) analysis

The production of  $\cdot\text{OH}$  by the UV-illuminated  $\text{Pt}/\text{TiO}_2$ ,  $\text{Pt}/\text{CeO}_2$ ,  $\text{Pt}/\text{SiO}_2$  catalysts was assessed using a photoluminescence (PL) method with coumarin as the probe molecule [45]. Coumarin readily reacts with  $\cdot\text{OH}$  to produce a highly fluorescent product, 7-hydroxycoumarin (7HC) (Fig. S1). The experimental procedure was similar to the photocatalytic activity measurements described in Section 2.4, except that 50 ml of water was replaced by 50 ml of coumarin aqueous solution ( $5 \times 10^{-4}$  M). Samples were collected at 5 min intervals and filtered through a membrane filter. The PL spectra of the generated 7HC were monitored at  $\lambda_{\text{max}} = 456$  nm when excited at  $\lambda_{\text{exc}} = 332$  nm. Fluorescence spectra were measured using a FluoroMax-4 (Horiba Jobin Yvon) spectrofluorometer.

### 2.6. Superoxide radical ( $\cdot\text{O}_2^-$ ) analysis

Superoxide radicals generated during the illumination of aqueous suspensions of Pt supported on the three metal oxides were examined using a nitro blue tetrazolium (NBT) degradation approach [46]. NBT shows a maximum absorbance at 259 nm and in the presence of superoxide radicals is converted into mono-formazan and di-formazan (Fig. S2). Superoxide radical production was quantitatively analyzed by detecting the concentration of NBT using UV-vis spectroscopy (Shimadzu UV-3600 spectrophotometer). The experimental procedure was similar to the photocatalytic activity test described in Section 2.4, with NBT solution replacing the aqueous phase. After 30 min of UV-light irradiation, the reaction solution was filtered and the decrease in NBT concentration was measured.

## 3. Results and discussion

### 3.1. Catalyst characteristics

Representative TEM images of the three supported Pt catalysts are shown in Fig. 1. For the  $\text{TiO}_2$  support (Fig. 1a), the Pt deposits have a narrow size distribution ranging from 1 to 5 nm (Fig. 1b) with the average size being 1.7 nm. The Pt deposits on the  $\text{SiO}_2$  support (Fig. 1c) ranged in size from 1 to 18 nm in diameter (Fig. 1d) with an average size of 4.4 nm. Discrete Pt particles from the TEM images of the  $\text{CeO}_2$

supported catalyst (Fig. 1e) were not identified. The actual Pt loadings on the  $\text{TiO}_2$ ,  $\text{SiO}_2$  and  $\text{CeO}_2$  supports were found from ICP-AES to be 0.75, 0.68 and 0.6 at%, respectively.

The  $\text{H}_2$ -TPR profiles for the Pt/metal oxide catalysts are shown in Fig. 2a. For  $\text{Pt}/\text{SiO}_2$ , the reduction of Pt species takes place in two steps at 105 °C and 162 °C, which is attributed to the reduction of  $\text{Pt}^{4+}$  to  $\text{Pt}^{2+}$  and  $\text{Pt}^{2+}$  to  $\text{Pt}^0$ , respectively. For the  $\text{Pt}/\text{CeO}_2$  and  $\text{Pt}/\text{TiO}_2$  catalysts, a broad peak across the 100 °C to 200 °C range is also attributed to Pt oxide reduction. It is known that the presence of Pt deposits promotes the reduction of  $\text{CeO}_2$  [47] and  $\text{TiO}_2$  [48] via a spill-over of hydrogen from Pt to the supports. Here, the effect occurs at temperatures of 341 °C and 326 °C, respectively, and represents the reduction of  $\text{CeO}_2$  and  $\text{TiO}_2$  resulting the formation of  $\text{Ce}^{3+}$  and  $\text{Ti}^{3+}$ , respectively [47,48]. The  $\text{H}_2$ -TPR results show that the 500 °C hydrogenation temperature used during catalyst preparation promotes a metallic Pt presence on the catalyst.

UV-vis spectra of the neat metal oxide and Pt/metal oxide catalysts, collected at ambient conditions, are shown in Fig. 2b. No significant differences between the spectra were observed for the wavelengths below 400 nm in which the characteristic sharp absorption thresholds of  $\text{TiO}_2$  and  $\text{CeO}_2$  at approximately 350 nm are observed. The weak absorption band of  $\text{Pt}/\text{SiO}_2$  in the range 200–300 nm is assigned to surface defects on the silica materials, that is, non-bridging oxygen hole centers accompanied by an E'center [49,50]. At the higher wavelengths, the spectra demonstrate a change in light absorption characteristics resulting from the deposition of Pt on the metal oxide supports. A broad absorption peak is apparent for  $\text{Pt}/\text{CeO}_2$  and  $\text{Pt}/\text{SiO}_2$  over the range of 400–550 nm, slightly decreasing as a function of increasing wavelength. However, for the  $\text{Pt}/\text{TiO}_2$  sample, the absorption intensities in the visible light range were significantly higher between 400 and 600 nm compared to neat  $\text{TiO}_2$ , and compared to  $\text{Pt}/\text{SiO}_2$  and  $\text{Pt}/\text{CeO}_2$ . This may arise from a strong interaction between the Pt and the  $\text{TiO}_2$  support [51]. In addition, the shift in absorption by  $\text{Pt}/\text{TiO}_2$  towards the visible light region is due to the generation of additional energy levels within the band gap of  $\text{TiO}_2$  [52] and overlapping of the original  $\text{TiO}_2$  band gap excitation with the plasmon band of the Pt nanoparticles [53]. Based on the UV-vis analysis, the band gaps of  $\text{TiO}_2$ ,  $\text{CeO}_2$ ,  $\text{Pt}/\text{TiO}_2$  and  $\text{Pt}/\text{CeO}_2$  were calculated to be 3.27, 3.32, 3.15, and 3.22, respectively. After depositing Pt, a slight red shift in the optical absorption edges was observed which has been previously reported by Li, et al. [52].

Fig. 3 depicts the XRD patterns of the neat  $\text{TiO}_2$ ,  $\text{SiO}_2$ ,  $\text{CeO}_2$ ,  $\text{Pt}/\text{TiO}_2$ ,  $\text{Pt}/\text{SiO}_2$  and  $\text{Pt}/\text{CeO}_2$ . The XRD pattern of neat  $\text{TiO}_2$  P25 displays peaks at 25.3° and 27.4° which are characteristic peaks for the anatase and rutile phases, respectively [54]. For neat  $\text{SiO}_2$ , the sharp XRD peaks at 20.8° and 26.6° correspond to (100) and (011) reflections of quartz silica [55]. The XRD patterns of  $\text{Pt}/\text{TiO}_2$  and  $\text{Pt}/\text{SiO}_2$  exhibit peaks at  $2\theta = 39.7^\circ$  and  $46.4^\circ$ , which can be attributed to Pt (111) and Pt (200), respectively (indexed according to JCPDF 01-1194) (Fig. S3). The Pt deposits possessed a face-centered cubic (fcc) structure with a Fm3m space group. It is worth noting that the Pt(111) and Pt(200) peaks were the sharpest and most distinct for the  $\text{Pt}/\text{SiO}_2$  sample (Fig. S3). The XRD patterns of neat  $\text{CeO}_2$  and  $\text{Pt}/\text{CeO}_2$  were indexed to the pure cubic phase Fm3m space group (according to JCPDS-34-0394) of  $\text{CeO}_2$ . No additional XRD peak attributable to Pt was apparent for  $\text{Pt}/\text{CeO}_2$ . This may be due to the Pt being present as very small, highly dispersed Pt deposits on the  $\text{CeO}_2$  which is in agreement with the TEM result.

### 3.2. Catalytic performance

Fig. 4 provides the  $R_{50}$  values for formic acid (FA) oxidation by the neat metal oxides ( $\text{TiO}_2$ ,  $\text{CeO}_2$  and  $\text{SiO}_2$ ) and Pt/metal oxide catalysts ( $\text{Pt}/\text{TiO}_2$ ,  $\text{Pt}/\text{CeO}_2$  and  $\text{Pt}/\text{SiO}_2$ ) under dark, pre-30 and photocatalytic conditions. The  $R_{50}$  value is defined as the rate for oxidizing 50% of formic acid to  $\text{CO}_2$ . As can be seen in Fig. 4, under dark conditions the neat metal oxides are all capable of oxidizing FA, albeit at a low rate. To

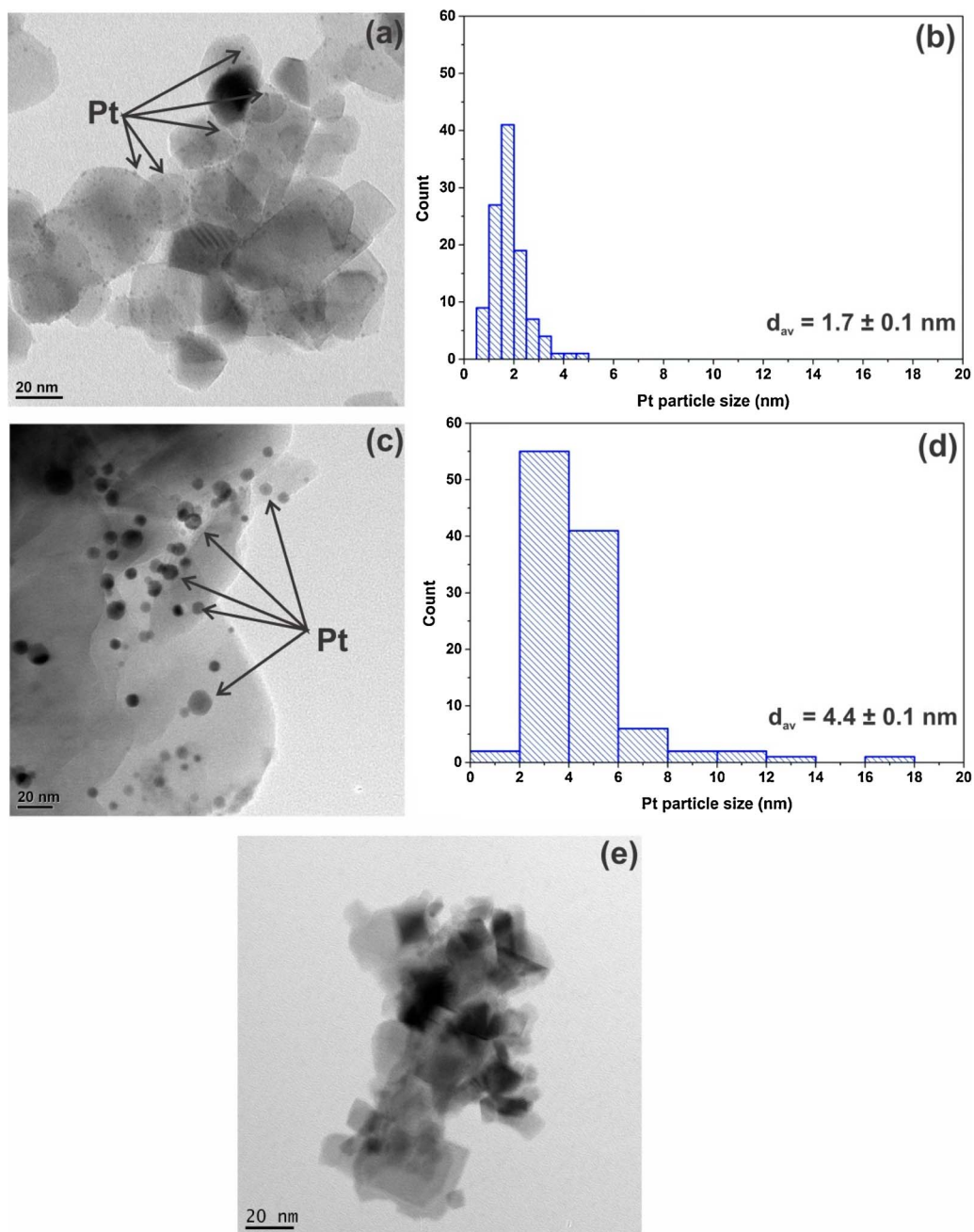


**Fig. 1.** TEM micrographs of (a) Pt/TiO<sub>2</sub> (c) Pt/SiO<sub>2</sub> (e) Pt/CeO<sub>2</sub> and size distribution of the platinum deposits on (b) Pt/TiO<sub>2</sub> (d) Pt/SiO<sub>2</sub>. Total number of Pt deposits counted per catalyst = 100.

confirm that the FA oxidation in this instance was not an artefact of the system, a control experiment was run in the dark and in the absence of the metal oxides whereby no FA degradation was observed. The activity displayed by the neat metal oxides suggests the supports are capable of activating oxygen to some extent. Light pre-treatment of the neat metal oxides does little to improve their activity. Oxygen defect generation on the surface of metal oxide supports was considered as responsible for improving the activity under the light pre-treatment condition. Our previous findings [40] suggested that the predominant effect of light pre-treatment was to alter the surface of the Pt and the TiO<sub>2</sub> support, in particular with the formation of Ti<sup>3+</sup> states. The Ti<sup>3+</sup> states, associated with oxygen vacancies, are able to trap photogenerated electrons which further activate oxygen on the TiO<sub>2</sub> surface. Furthermore, UV light illumination greatly enhances the rate of FA oxidation for the neat TiO<sub>2</sub> and CeO<sub>2</sub>. The photocatalytic activity displayed by the neat TiO<sub>2</sub> and CeO<sub>2</sub> derives from their semiconducting nature while the lack of photocatalytic improvement for the neat silica stems from its insulating

properties.

On adding Pt deposits to the metal oxide surface, the changes in R<sub>50</sub> are defined by the particular metal oxide support. For the Pt/TiO<sub>2</sub> catalyst, loading the Pt increased the activity in the dark while pre-treating the sample with UV light greatly improved its catalytic performance. Photocatalysis using the Pt/TiO<sub>2</sub> catalyst gave the best activity although it was only slightly better than the pre-illuminated case. Under the dark catalysis conditions, the Pt deposits are believed to activate oxygen in addition to the TiO<sub>2</sub> support. Pre-treating the Pt/TiO<sub>2</sub> with UV light is anticipated to have produced photogenerated electrons within the TiO<sub>2</sub> which were subsequently captured and scavenged by the Pt deposits where they were then available for FA oxidation. The electrons scavenged by the Pt deposits are transferred to (pre-adsorbed) oxygen molecules and as such are expected to facilitate oxygen dissociation to generate activated oxygen species and improve performance when compared to the pre-treated neat TiO<sub>2</sub> and the Pt/TiO<sub>2</sub> system without light pre-treatment. Under continuous UV

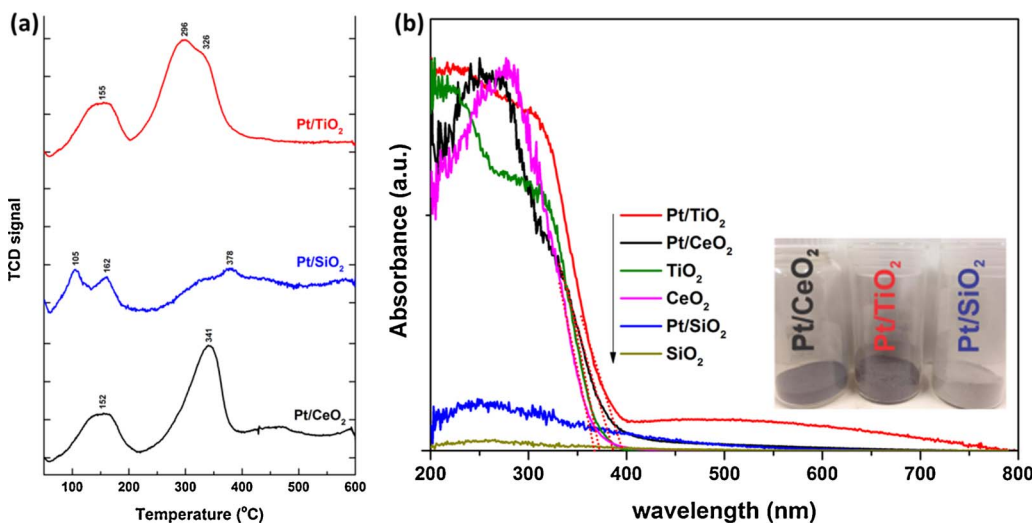


Fig. 2. (a) H<sub>2</sub>-TPR profiles of as prepared Pt/TiO<sub>2</sub>, Pt/SiO<sub>2</sub> and Pt/CeO<sub>2</sub> (b) UV-vis spectra of neat TiO<sub>2</sub>, SiO<sub>2</sub>, CeO<sub>2</sub>, Pt/TiO<sub>2</sub>, Pt/SiO<sub>2</sub> and Pt/CeO<sub>2</sub>.

illumination, additional reactive oxidative species including reactive holes, hydroxyl radicals and superoxide anion radicals are known to be generated by the TiO<sub>2</sub> which can further improve the activity. The presence of Pt is known to enhance the activity of illuminated semiconductors by improving electron hole separation by shuttling the electrons away from the metal oxide semiconductor, adsorbing more oxygen and generally producing a greater number of reactive oxidative species in the system.

For the Pt/CeO<sub>2</sub> system, UV pre-treatment was found to have a mild effect on the R<sub>50</sub> whereas under continuous illumination the R<sub>50</sub> was enhanced seven-fold. Despite the semiconducting nature of the CeO<sub>2</sub>, the existence of Pt oxides (i.e. absence of metallic Pt, from TEM analyses as shown in Fig. 1e and Supporting Information, Fig. S3) may account for the limited improvement in performance following light pre-treatment. This will be discussed in greater detail later on. For the continuously illuminated system, the photogenerated holes, electrons and other reactive oxygen species, arising from the semiconducting properties of CeO<sub>2</sub>, are believed to be the main contributors to the greater FA oxidation.

In the instance of Pt/SiO<sub>2</sub>, the R<sub>50</sub> under both the dark conditions and following UV light pre-treatment was the highest of the three Pt/

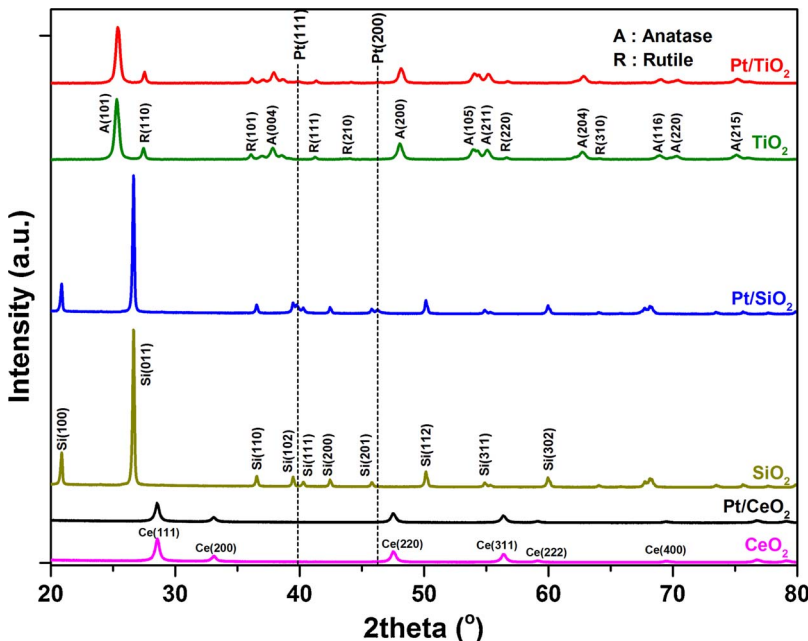


Fig. 3. XRD patterns of neat TiO<sub>2</sub>, SiO<sub>2</sub>, CeO<sub>2</sub>, Pt/TiO<sub>2</sub>, Pt/SiO<sub>2</sub> and Pt/CeO<sub>2</sub>.

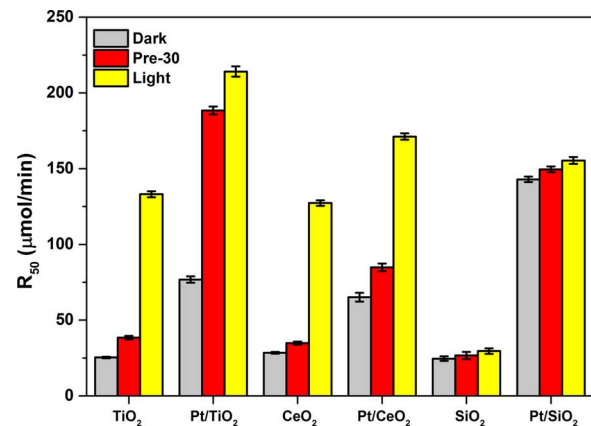
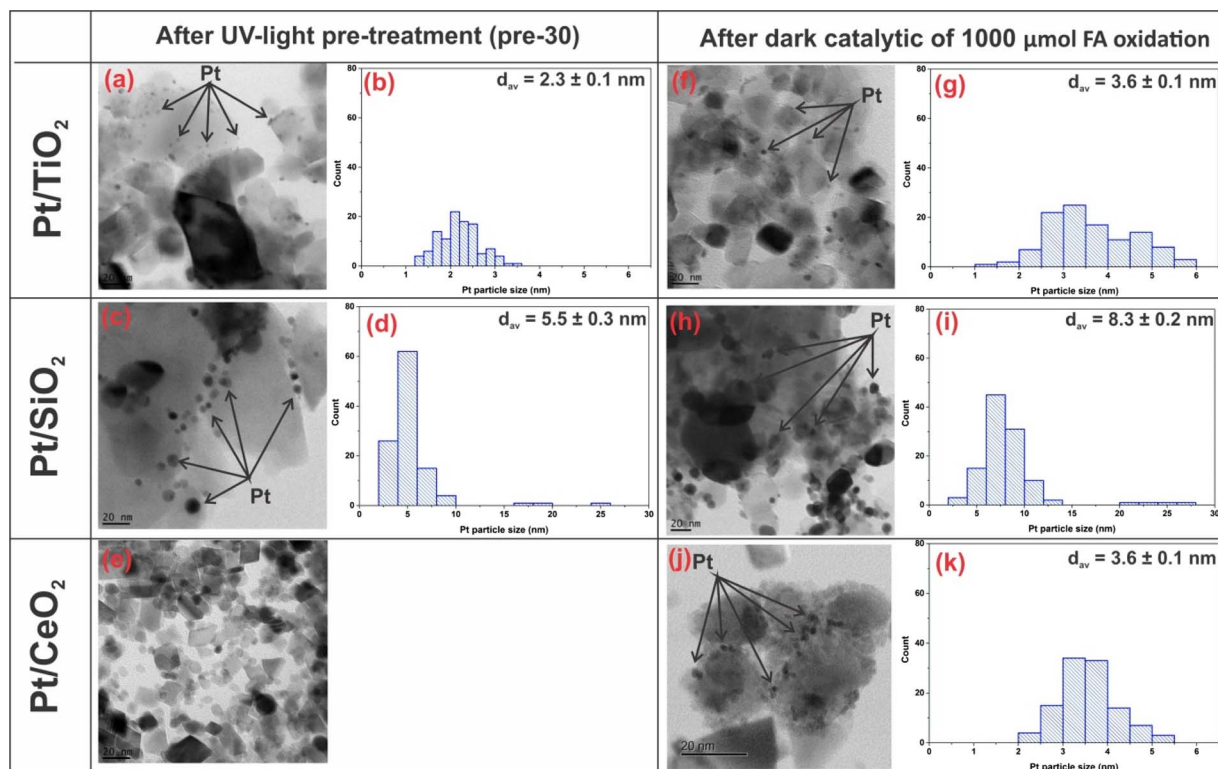


Fig. 4. Effect of metal oxide support on FA oxidation (R<sub>50</sub>) by the neat metal oxide and metal oxide-supported Pt catalysts under: dark (non-illuminated) catalysis conditions; pre-treated with UV light for 30 min (pre-30); and under photocatalytic conditions. Suspension volume = 50 ml; catalyst loading = 1 g/L; suspension pH = 3 ± 0.05; air equilibration time = 10 min; relaxation time = 10 min; initial FA loading = 1000 μmol.



**Fig. 5.** TEM images of Pt/metal oxide catalysts following UV light pre-treatment and subsequent dark catalytic oxidation of 1000  $\mu\text{mol}$  of FA. Also included are the size distributions of the Pt deposits (a, b, f, g) Pt/TiO<sub>2</sub>; (c, d, h, i) Pt/SiO<sub>2</sub>; (e, j, k) Pt/CeO<sub>2</sub>. Total number of Pt deposits counted per sample = 100.

metal oxides. As SiO<sub>2</sub> is an insulator, the R<sub>50</sub> of Pt/SiO<sub>2</sub> remained unchanged under photocatalytic conditions in contrast to the CeO<sub>2</sub> and TiO<sub>2</sub>. The better performance of Pt/SiO<sub>2</sub> compared to neat SiO<sub>2</sub> is thought to arise from the metallic Pt presence which promotes greater oxygen activation under dark catalysis conditions [41,56].

To explain the differences in reactivity between the Pt-loaded and neat metal oxides, especially under dark catalysis conditions, further characterization was conducted. The characterization tests focus on the as-prepared samples, the pre-30 samples and the samples post dark catalytic FA oxidation. TEM imaging was used to examine differences in Pt deposit shape and size while XPS analysis was used to study the oxidation states of Pt, O, Ti, Si, and Ce.

### 3.3. Catalyst morphology

Fig. 5 shows TEM micrographs and the accompanying Pt deposit size distributions for Pt/TiO<sub>2</sub>, Pt/SiO<sub>2</sub> and Pt/CeO<sub>2</sub> following just UV illumination pre-treatment and following UV illumination pre-treatment and then FA oxidation. The Pt deposit size distributions are based on approximately 100 particle counts for each sample. Fig. 6 shows HAADF HR-STEM images of the (i) as-prepared, (ii) after just UV-light pre-treatment and (iii) after UV light pre-treatment and catalytic oxidation of 1000  $\mu\text{mol}$  FA samples. Where obtainable, the inset in each HAADF HR-STEM image provides the associated fast Fourier transform (FFT) pattern indicating the crystal facet of the Pt deposits. As mentioned earlier, the average Pt deposit size on the as-prepared Pt/TiO<sub>2</sub> and Pt/SiO<sub>2</sub> was found to be 1.7 and 4 nm (Fig. 1), respectively. No discernible Pt deposits were observed in the TEM image of the Pt/CeO<sub>2</sub> sample (Fig. 1e). However, energy dispersive X-ray spectroscopy (EDS, Fig. S4a) and HAADF HR-STEM imaging (Fig. 6c) shows that Pt deposits of a very small size (< 1 nm) are distributed over the CeO<sub>2</sub> support surface. When comparing the average Pt deposit size of the as prepared samples and the pre-30 samples (Fig. 5), it is apparent that UV pre-treatment invokes a slight increase in the Pt deposit size on TiO<sub>2</sub> and SiO<sub>2</sub> support to 2.3 nm (Fig. 5a and b) and 5.5 nm (Fig. 5c and d),

respectively. No visible Pt deposits were observable on the pre-30 Pt/CeO<sub>2</sub> sample (Fig. 5e) while from EDS (Fig. S4b) and HAADF HR-STEM (Fig. 6f) analyses, very small Pt deposits (< 1 nm) were observed on the pre-30 Pt/CeO<sub>2</sub> sample. After the dark catalytic FA oxidation process, an increase in the size of the Pt deposits was apparent for both the Pt/TiO<sub>2</sub> (Fig. 5f) and Pt/SiO<sub>2</sub> (Fig. 5h) samples with average particle sizes of 3.6 and 8.3 nm, respectively. Interestingly, for the Pt/CeO<sub>2</sub> sample, Pt deposits were now observable in the TEM image (Fig. 5j) and the EDS spectrum (Fig. S4c). The ‘appearance’ of the Pt deposits on Pt/CeO<sub>2</sub> following FA oxidation is thought to derive from the FA acting as a reducing agent for ionic Pt<sup>4+</sup> and Pt<sup>2+</sup> species, leading to the formation of metallic Pt (average deposit size ~ 3.6 nm). Moreover, EDS mapping of the pre-30 Pt/TiO<sub>2</sub> (Fig. S5a), pre-30 Pt/SiO<sub>2</sub> (Fig. S5b) and of the Pt/CeO<sub>2</sub> after FA oxidation (Fig. S5c) confirmed the growth in Pt deposit size compared to the as-prepared catalysts. Other studies have reported the growth in Pt metal deposit size can instead be attributed to coalescence and aggregation, during UV illumination [57] and with catalyst recycling [58], the extent of which depends on a number of factors including the type of catalyst support, the heat treatment applied and aging of the samples. This is supported by extensive studies relating to the fundamental principles of nanoparticle formation [59].

The size and amount of Pt deposits can affect the oxidation reaction rate, whereby a large quantity of Pt deposits on the support as well as large deposits (relative to the size of the support) can potentially be blocked surface active sites affecting the activation of the semi-conducting support (i.e. generation of the active holes and electrons on the semiconductor support) by UV light [60]. Furthermore, if the charge carrier space distance is too small, the increase of electron-hole recombination rates was obtained [20]. In contrast, if the Pt deposit size is too small, a sufficient electrical contact cannot be established between metal deposit and support, resulting in inefficient charge transfer [61,62]. On inspecting TEM micrographs, although the size of the Pt deposits has not been optimized, the potentially detrimental impact of metal deposit size may have an effect on observed activities, given that an optimum Pt deposit size typically exists for a given reaction [63].

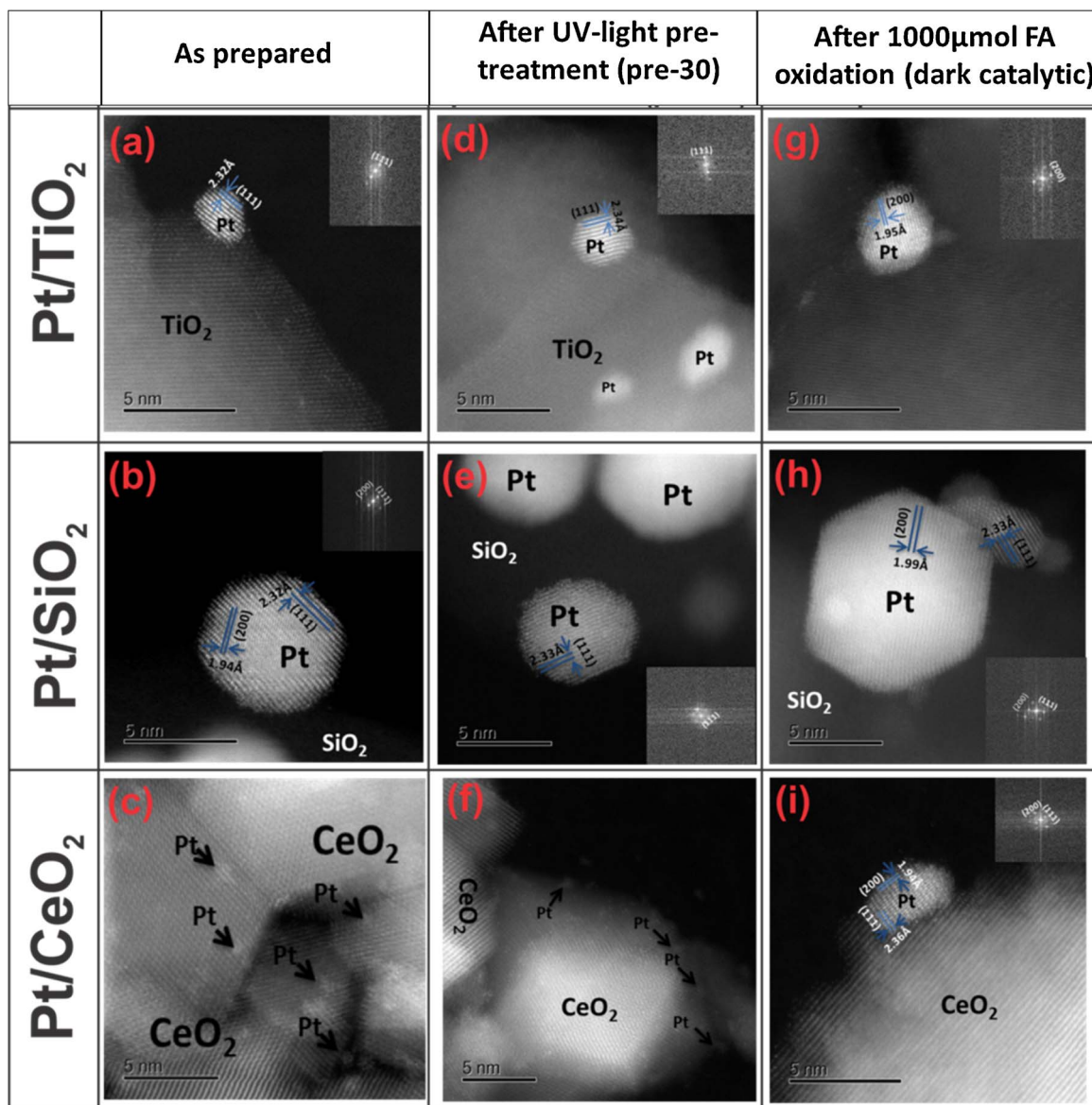


**Fig. 6.** HAADF HR-STEM images of as prepared Pt/metal oxide catalysts, following UV light pre-treatment and subsequent dark catalytic oxidation of 1000  $\mu\text{mol}$  FA (a, d, g) Pt/TiO<sub>2</sub>, (b, h) Pt/SiO<sub>2</sub> and (c, f, i) Pt/CeO<sub>2</sub>. The inset in each HAADF HR-STEM image depicts the associated fast Fourier transform (FFT) pattern.

As mentioned earlier, the Pt deposit shape and its exposed crystal facets may affect the degree of activation of oxygen species [17], and hence may play a role in defining the FA oxidation rate. Tian et al. [64] demonstrated that a high-index facet of Pt nanoparticles containing under-coordinated surface atoms, resulted in a four-fold enhancement in ethanol oxidation. From the HAADF HR-STEM images in Fig. 6, it can be seen that the Pt deposit shape on the TiO<sub>2</sub> (Fig. 6a, d, and g) and CeO<sub>2</sub> (Fig. 6c, f, and i) supports is mainly hemispherical, while on the SiO<sub>2</sub> support (Fig. 6b, e, and h) the deposit shape is predominantly cubooctahedral. Ngandjou et al. [65], on simulating silver cluster formation and silver deposition on substrates such as amorphous silica (which typically exhibits a weak interaction with metal clusters) reported that the formation of metal deposits as truncated octahedrons was favored. A similar effect appears to be evident for our Pt deposits on the silica particles.

It has been reported that a hexagonal Pt deposit shape comprising of both Pt single crystal (111) and (100) surface facets exhibited the highest activity for catalyzing the ORR compared to other shapes such as spherical, cubic, and tetrahedral-octahedral [14]. Kinoshita et al. [66] reported that the change in the fraction of surface atoms on the Pt

(100) and Pt (111) crystal planes was crucial for obtaining a high ORR activity. The lattice measurements of the as prepared and pre-30 Pt catalyst here show the Pt lattice fringes for Pt/SiO<sub>2</sub> (Fig. 6b and e) are 1.94 Å and 2.32 Å, which correspond to the Pt(200) and Pt(111) facets. On the Pt/TiO<sub>2</sub> (Fig. 6a and d) the presence of Pt(111) was confirmed with a lattice fringe of 2.32 Å. The Pt facets identified from the HAADF HR-STEM analysis agree with the XRD results (Fig. S3) where the Pt (111) and Pt (200) peaks were observed to be sharper and more pronounced for the as-prepared Pt/SiO<sub>2</sub> sample compared to the as-prepared Pt/TiO<sub>2</sub>. The findings suggest that the comparatively high FA oxidation rate exhibited by the Pt/SiO<sub>2</sub> under the dark catalysis condition may be a consequence of the cubooctahedral Pt deposits possessing Pt(111) and Pt(200) facets. The Pt deposit size on the as-prepared and pre-30 Pt/CeO<sub>2</sub> samples was too small to be able to reliably quantify the lattice fringe of the Pt deposits. After the dark catalytic oxidation of 1000  $\mu\text{mol}$  FA, Pt deposits were observed on the CeO<sub>2</sub> support with lattice fringes of 2.36 Å and 1.94 Å (Fig. 6i) which correspond to Pt(111) and Pt(200).

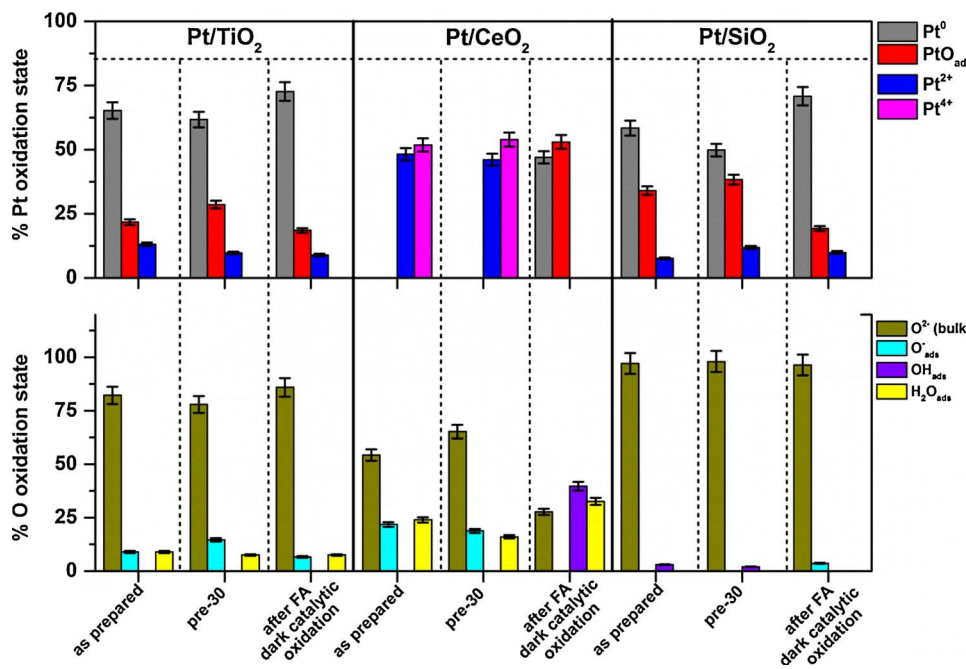


Fig. 7. The relative proportions of Pt and O species as observed from the Pt4f and O1s core level XPS spectra in Pt/TiO<sub>2</sub>, Pt/SiO<sub>2</sub> and Pt/CeO<sub>2</sub> for the as-prepared samples, the samples after 30 min UV illumination pre-treatment (pre-30) and after the ensuing dark catalytic oxidation of 1000 μmol FA. The standard error was estimated to be ± 5% [67].

### 3.4. XPS analysis

To further explain the differences in reactivities of the Pt-loaded and neat metal oxides, especially under dark catalysis conditions, XPS analysis was conducted to investigate the surface oxidation states of the Ti2p, Ce3d, Si2p, O1s and Pt4f core levels. The XPS results are summarized in Fig. 7 with the original spectra provided in Figs. S6–S8. Four separate Pt species were observed in the samples (Fig. S6): (i) metallic Pt (Pt<sup>0</sup>); (ii) atomic oxygen species adsorbed on the Pt surface (PtO<sub>ads</sub>); and oxidized Pt in the (iii) +2 (Pt<sup>2+</sup>) and (iv) +4 (Pt<sup>4+</sup>) states. Four separate oxygen species at the O1s core level (Fig. S7) were also observed: (i) oxygen in the bulk system (O<sup>2-</sup> bulk); (ii) adsorbed oxygen (O<sub>ads</sub>); (iii) adsorbed hydroxyl groups (OH<sub>ads</sub>); and (iv) adsorbed water molecules (H<sub>2</sub>O<sub>ads</sub>). The relative proportions of the Pt and O species for the as-prepared Pt/TiO<sub>2</sub>, Pt/SiO<sub>2</sub> and Pt/CeO<sub>2</sub> samples, the same samples after UV illumination pre-treatment (pre-30) and after the subsequent dark catalytic oxidation of 1000 μmol FA are presented in Fig. 7.

For the Pt/TiO<sub>2</sub> sample, Pt<sup>0</sup>, PtO<sub>ads</sub> and Pt<sup>2+</sup> were observed while O<sup>2-</sup> bulk, O<sub>ads</sub> and H<sub>2</sub>O<sub>ads</sub> at O1s core level were observed at each reaction condition. The relative amount of PtO<sub>ads</sub> and O<sub>ads</sub> slightly increased for the pre-30 sample (compared to the as-prepared case), with a concomitant decrease in the Pt<sup>0</sup>, Pt<sup>2+</sup>, and O<sup>2-</sup> bulk. Additionally, almost all the Pt peaks shifted to a lower binding energy (indicating a higher electron density in the Pt) compared to the as-prepared sample (Fig. S6a). Following FA oxidation, both the PtO<sub>ads</sub> and O<sub>ads</sub> had decreased which was accompanied by a slight increase in Pt<sup>0</sup>. In addition, at the Ti2p core level, a slight shift in the 459 eV peak (which corresponds to Ti<sup>4+</sup>) to a lower binding energy was observed for both the pre-30 sample and the sample following the dark catalytic reaction (Fig. S8a). It is apparent that for the Pt/TiO<sub>2</sub> catalyst, surface active oxygen species (PtO<sub>ads</sub> and O<sub>ads</sub>) are consumed during the FA oxidation process. The UV pre-illumination treatment step increases the PtO<sub>ads</sub> and O<sub>ads</sub> by around 4–6% which is believed to be responsible for the elevated activity. That is, light pre-treatment enhances the electron density within the Pt deposits and when coupled with an (adsorbed) oxygen-rich environment greater molecular oxygen dissociation and activation is promoted, in turn enhancing the FA oxidation rate.

In the instance of the Pt/SiO<sub>2</sub> sample, Pt<sup>0</sup>, PtO<sub>ads</sub> and Pt<sup>2+</sup> were also observed for the as prepared and the pre-30 samples. UV pre-treatment

slightly increased the PtO<sub>ads</sub> and Pt<sup>2+</sup> which was accompanied by a slight decrease in Pt<sup>0</sup>. During FA oxidation, there is a substantial increase in Pt<sup>0</sup> with a concomitant decrease in PtO<sub>ads</sub> and Pt<sup>2+</sup>. At the O1s core level, the most dominant species was O<sup>2-</sup> bulk while a small proportion of OH<sub>ads</sub> was observed for the as-prepared and pre-30 samples. Following FA oxidation an additional peak at 530.6 eV was observed which corresponded to O<sub>ads</sub><sup>2-</sup> accompanied by a decrease in OH<sub>ads</sub>. The Si2p spectra of Pt/SiO<sub>2</sub> (Fig. S8b) are dominated by a peak centered at a binding energy of 103.0–103.7 eV. This is characteristic of Si<sup>4+</sup> in SiO<sub>2</sub>. The peak slightly shifted to a lower binding energy after UV pre-treatment and after the FA oxidation reaction compared to the as-prepared sample, indicating a change in the chemical environment of the Si–O–Si bonds. The findings suggest Pt<sup>0</sup> and PtO<sub>ads</sub> play a key role during the FA oxidation reaction over Pt/SiO<sub>2</sub>.

For the Pt/CeO<sub>2</sub> sample, only Pt<sub>ox</sub> (Pt<sup>2+</sup> and Pt<sup>4+</sup>) was observed while no Pt<sup>0</sup> and no PtO<sub>ads</sub> were detected for the as-prepared and pre-30 samples. The absence of Pt<sup>0</sup> may be due to CeO<sub>2</sub> being an active support for precious metals, whereby such metal deposits have been reported to be spontaneously oxidized [68]. In addition, the strong metal-support interaction between Pt and CeO<sub>2</sub> may contribute to the reduction/decomposition of the Pt deposits which depends on the morphology of the CeO<sub>2</sub> itself [69]. However, the CeO<sub>2</sub> morphology, as observed from TEM (Fig. 5e) and HAADF-STEM (Fig. 6c) was octahedral with the predominant Pt state being the oxide (i.e. Pt<sup>2+</sup> and Pt<sup>4+</sup>) (which is not in complete agreement with the findings by Gao, et al. [69]). Furthermore, as the presence of Pt<sup>0</sup> and PtO<sub>ads</sub> are key for oxygen dissociation and activation, the absence of both species in the Pt/CeO<sub>2</sub> accounts for its low activity for dark catalysis, both with and without UV pre-treatment. From the XPS profiles, it can be seen that after the FA oxidation reaction, Pt<sup>0</sup> and PtO<sub>ads</sub> are present on the Pt/CeO<sub>2</sub>, which are generated during the FA oxidation process. FA is a known reducing agent and appears to be capable of reducing the Pt oxides in this instance. XPS analysis at the O1s core level showed three different species including O<sup>2-</sup> bulk, O<sub>ads</sub> and H<sub>2</sub>O<sub>ads</sub> for the as-prepared and pre-30 samples while, during the FA oxidation reaction, O<sub>ads</sub> disappears accompanied by an increase in OH<sub>ads</sub>. At the Ce3d core level (Fig. S8c), two peaks at 917.2 and 898.6 eV were the main lines for the Ce3d<sub>3/2</sub> and Ce3d<sub>5/2</sub> states, respectively, and correspond to the final state of the 3d<sup>10</sup>4f<sup>0</sup> configuration of Ce<sup>4+</sup> ions. Each of the main lines has two satellite peaks at 907.4 eV, 901.5 eV and 888.6 eV, 882.9 eV located at

**Table 1**

Relative amounts of  $\text{Ce}^{3+}$  and  $\text{Ce}^{4+}$  (from XPS) and their ratios for the as-prepared  $\text{Pt}/\text{CeO}_2$  sample, after UV illumination pre-treatment (pre-30) and after the dark catalytic oxidation of 1000  $\mu\text{mol}$  of FA.

Sample-treatment	Relative proportion (%)		$\text{Ce}^{3+}/\text{Ce}^{4+}$
	$\text{Ce}^{4+}$	$\text{Ce}^{3+}$	
$\text{Pt}/\text{CeO}_2$ as-prepared	72.1	27.9	0.39
$\text{Pt}/\text{CeO}_2$ pre-30	64.2	35.8	0.56
$\text{Pt}/\text{CeO}_2$ after dark catalytic reaction (1000 $\mu\text{mol}$ FA)	94.7	5.3	0.06

the lower binding energy side of the main peak and are due to the bonding and antibonding states arising from the transfer of one or two electrons from a filled  $\text{O}2\text{p}$  orbital to an empty  $\text{Ce}4\text{f}$  orbital. The peaks at 904.1 eV and 885.5 eV represent the  $3\text{d}^{10} 4\text{f}^1$  initial electronic state of the  $\text{Ce}^{3+}$  ions. The presence of all these peaks indicates the co-existence of  $\text{Ce}^{4+}$  and  $\text{Ce}^{3+}$  ions on the surface of the  $\text{Pt}/\text{CeO}_2$  catalyst. Such an observation is important as it provides evidence suggesting FA oxidation follows the Mars-van Krevelen mechanism on  $\text{Pt}/\text{CeO}_2$  catalysts, under dark catalytic conditions [68].

In Table 1, the relative amounts of  $\text{Ce}^{3+}$  and  $\text{Ce}^{4+}$  and their ratios are presented. As can be seen from the Table, the original sample had a high proportion of  $\text{Ce}^{4+}$  which decreased with the pre-illumination step as was expected given the production of photogenerated electrons which reduce  $\text{Ce}^{4+}$  to  $\text{Ce}^{3+}$  [70]. After the reaction however, the amount of  $\text{Ce}^{3+}$  in the sample decreased significantly. It is known that the Mars-van Krevelen mechanism of catalytic oxidation explicitly involves a redox process in which oxygen at the catalyst surface is consumed and act as the active oxygen species [71]. The mechanism is especially important for metal oxide catalysts that are readily reducible such as  $\text{TiO}_2$  and  $\text{CeO}_2$ . Hence, under the dark catalytic oxidation conditions, it is believed that the oxygen vacancies associated with  $\text{Ce}^{3+}$  are important for FA oxidation. It should be noted, though that the  $R_{50}$  for FA oxidation using the  $\text{Pt}/\text{CeO}_2$  catalyst under dark catalysis conditions with and without UV pre-treatment was not high compared to  $\text{Pt}/\text{TiO}_2$  and  $\text{Pt}/\text{SiO}_2$ . This is believed to be due to the lack of metallic Pt initially on the  $\text{Pt}/\text{CeO}_2$  and indicates that the mechanism involving oxygen dissociation and activation supersedes the mechanism involving the  $\text{Ce}^{3+}$  and  $\text{Ce}^{4+}$  redox couple. The octahedral  $\text{CeO}_2$  does not appear to be the ideal support for Pt, when prepared by the impregnation method, as the metallic state of Pt was not obtained.

To better understand the roles of  $\text{Pt}^0$  and surface active oxygen ( $\text{PtO}_{\text{ads}}$  and  $\text{O}_{\text{ads}}^-$ ) species in the oxidation process, the  $\text{Pt}/\text{metal oxide}$  catalyst samples were collected after an initial 1000  $\mu\text{mol}$  FA dark catalytic oxidation cycle, pre-treated with UV light and then recycled for a second 1000  $\mu\text{mol}$  FA dark catalytic oxidation reaction. The results

are presented in Fig. S9 with the repeat catalytic runs labelled as '2nd cycle'. In Fig. S9 it can be seen that recycling leads to a decrease in the  $R_{50}$  for  $\text{Pt}/\text{TiO}_2$  and  $\text{Pt}/\text{SiO}_2$ , while there is an approximately four-fold increase in the  $R_{50}$  for the  $\text{Pt}/\text{CeO}_2$ . Also included in Fig. S9 is the relative amount of  $\text{PtO}_{\text{ads}}$ , which follows the same trend observed for  $R_{50}$  for all the catalysts. The findings suggest the increase in the  $\text{Pt}/\text{CeO}_2$  activity for the second cycle derives from the increase in  $\text{PtO}_{\text{ads}}$ , reaffirming the importance of this species for the oxidation activity. The minor loss in activity observed for the  $\text{Pt}/\text{TiO}_2$  and  $\text{Pt}/\text{SiO}_2$  samples on the second cycle is suspected to arise from a partial loss of these species, possibly due to an increase in deposit size upon recycling [58,72] or a general decrease in the catalyst surface area upon recycling [72,73]. The results confirm that the surface active oxygen species comprising  $\text{PtO}_{\text{ads}}$  and  $\text{O}_{\text{ads}}^-$  are key oxidative species during the dark catalysis with and without UV pre-treatment. Based on the observations for the three  $\text{Pt}/\text{metal oxide}$  catalysts it is apparent that two factors have an impact on the dark catalytic FA oxidation process; (i) Pt deposit characteristics such as size and shape; and (ii) the Pt oxidation state.

### 3.5. Reactive oxygen species (ROS) generation during the photocatalytic reaction

To further comprehend the processes occurring during the photocatalytic reaction over each of the catalysts and how they differed from the dark catalytic reactions, hydroxyl radical ( $\cdot\text{OH}$ ) and superoxide anion radical ( $\cdot\text{O}_2^-$ ) generation was studied under photocatalytic conditions using PL and UV-vis spectroscopy, respectively. The  $\cdot\text{OH}$  yield after 30 min UV light irradiation for each support and Pt-based catalyst is presented in Fig. 8a. The amount of  $\cdot\text{OH}$  was found to decrease in the order  $\text{Pt}/\text{TiO}_2 > \text{Pt}/\text{CeO}_2 > \text{TiO}_2 > \text{CeO}_2 > > \text{Pt}/\text{SiO}_2 > \text{SiO}_2$ . Additionally, on increasing the illumination time an exponential increase in the  $\cdot\text{OH}$  presence was observed (Fig. S10a). The photocatalytic properties of, both neat  $\text{TiO}_2$  and  $\text{CeO}_2$  promote  $\cdot\text{OH}$  generation upon UV illumination, which is then amplified when Pt is loaded on their surface (Fig. S10a). In contrast, in the case of  $\text{SiO}_2$ , minimal  $\cdot\text{OH}$  generation occurred upon UV illumination.

Fig. 8b depicts the NBT transformation (to monitor the generation of  $\cdot\text{O}_2^-$ ) by the neat metal oxides and the Pt/metal oxide catalysts after 30 min of UV light treatment. The NBT undergoes a degree of degradation with an increase in UV illumination time (Fig. S10b), in particular for the  $\text{CeO}_2$  and  $\text{TiO}_2$ , while only a small loss was observed for the  $\text{SiO}_2$ . The amount of generated  $\cdot\text{O}_2^-$  was found to decrease in the order of  $\text{Pt}/\text{TiO}_2 > \text{TiO}_2 > \text{Pt}/\text{CeO}_2 > \text{CeO}_2 > > \text{Pt}/\text{SiO}_2 > \text{SiO}_2$ . The higher amount of  $\cdot\text{O}_2^-$  generated by both  $\text{Pt}/\text{TiO}_2$  and  $\text{Pt}/\text{CeO}_2$  compared to the neat metal oxides, confirms the ability of Pt to accumulate the photo-generated electrons and transfer them to adsorbed  $\text{O}_2$ . Furthermore, to highlight the requirement of a photocatalyst for

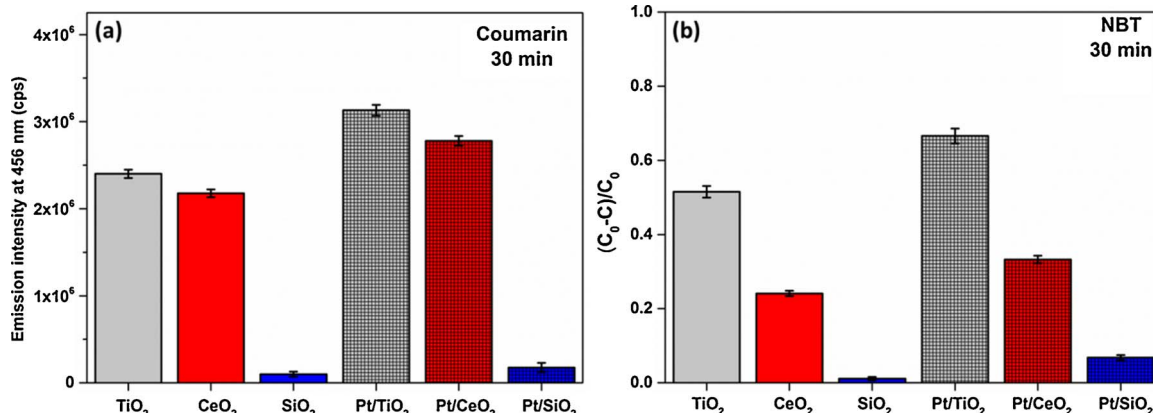
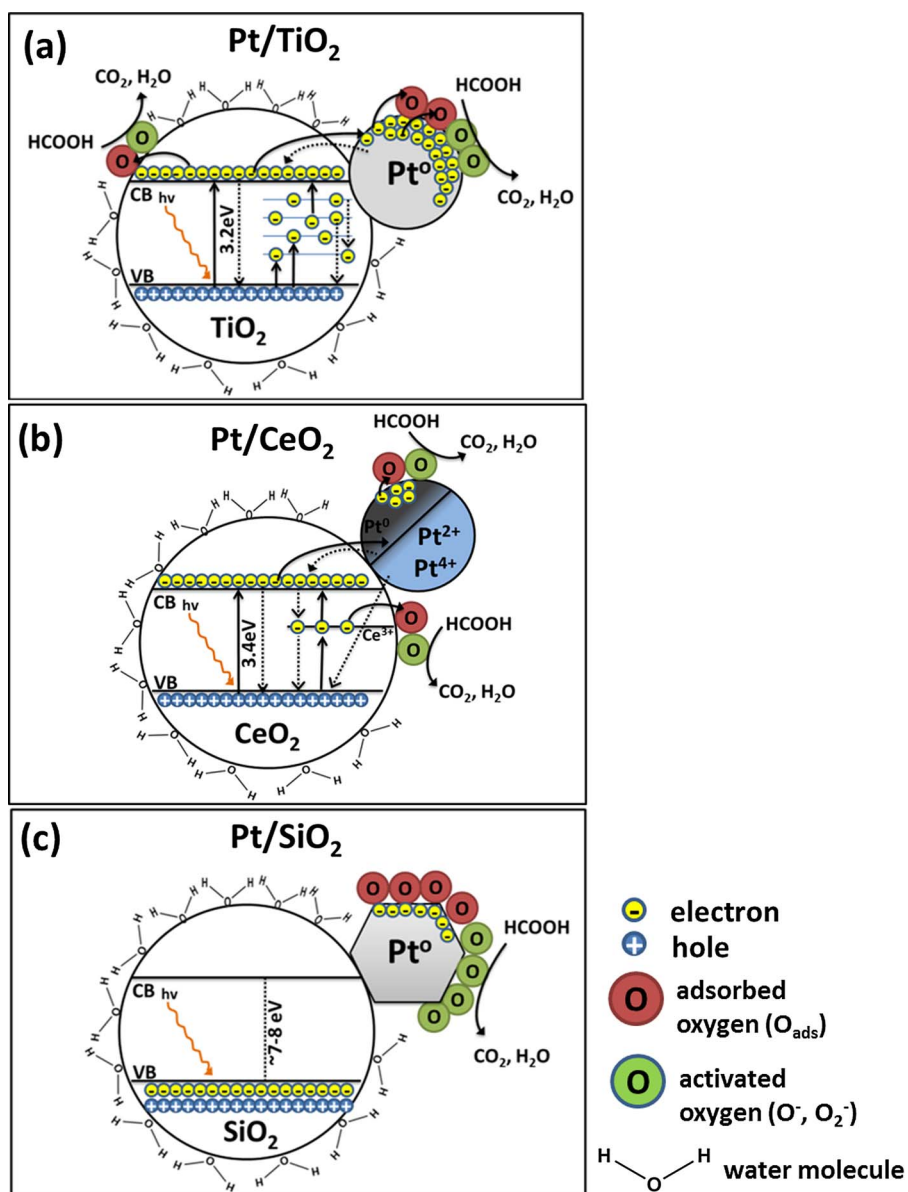


Fig. 8. The changes in emission intensity measured at 455 nm in aqueous phase under photolysis of coumarin (b) transformation percentage of NBT within 30 min UV light illumination by neat metal oxides and Pt/metal oxide catalysts.



**Fig. 9.** Schematic detailing the mechanisms for dark catalytic FA oxidation using UV light pre-treated (a) Pt/TiO<sub>2</sub>, (b) Pt/CeO<sub>2</sub> and (c) Pt/SiO<sub>2</sub>.

generating hydroxyl and superoxide radicals, control tests were performed in the absence of a photocatalyst as shown in Fig. S11. A maximum PL emission and absorption of  $2.1 \times 10^4$  counts/s (Fig. S11a and S11b) and 0.05 a.u (Fig. S11c and S11d) were observed, respectively, which is considered to be minor.

### 3.6. Proposed mechanism

Based on the findings and associated discussion presented previously, a schematic depicting the possible reaction mechanisms for the dark catalytic FA oxidation (with UV pre-treatment) for Pt/TiO<sub>2</sub>, Pt/CeO<sub>2</sub> and Pt/SiO<sub>2</sub> are presented in Fig. 9. The mechanism proposed for Pt/TiO<sub>2</sub> is detailed in Fig. 9a. Based on the XPS results, which showed that there were more PtO<sub>ads</sub> species following UV pre-treatment, electron transfer from the TiO<sub>2</sub> CB to the Pt deposits is believed to occur during this step leading to an increase in activated oxygen on the Pt surface. The results agree with our previous works [40,41] with the activated oxygen species then thought to play a role during the FA oxidation reaction.

In the case of the Pt/CeO<sub>2</sub> system (Fig. 9b), the O<sub>2</sub> molecules are believed to adsorb on the surface while also being able to migrate into the

CeO<sub>2</sub> lattice to fill any oxygen vacancies. The adsorbed oxygen species can subsequently interact with FA forming CO<sub>2</sub> and H<sub>2</sub>O. On pre-treating the catalyst with UV light a reduction of Ce<sup>4+</sup> to Ce<sup>3+</sup> occurs via the injection of electrons from the conduction band of CeO<sub>2</sub> forming additional oxygen vacancies. Although Pt<sub>ox</sub> can also trap electrons from the conduction band of CeO<sub>2</sub> (which can be subsequently transferred to adsorbed oxygen), Pt<sub>ox</sub> may also act as a recombination center [21]. Thus, despite the absence of Pt<sup>0</sup> and PtO<sub>ads</sub> in the as-prepared Pt/CeO<sub>2</sub>, the adsorbed oxygen together with surface Ce<sup>3+</sup> on CeO<sub>2</sub> and lattice oxygen vacancies can potentially oxidise FA in the dark via the Mars van Krevelen mechanism [74].

For the Pt/SiO<sub>2</sub> system, Pt<sup>0</sup> and PtO<sub>ads</sub> are believed to be vital species for the dark catalytic FA oxidation (Fig. 9c), similar to the Pt/TiO<sub>2</sub> system. Adsorbed oxygen on the Pt and SiO<sub>2</sub> surface is thought to come from the disproportionation of adsorbed water and oxygen [75,76]. Isolated hydroxyl groups may also diffuse easily across the Pt surface to form adsorbed oxygen [77]. Moreover, the silanol group (Si—OH) density as well as the circumference of the Pt/SiO<sub>2</sub> interface have been reported as key factors affecting the charge transfer between Pt and SiO<sub>2</sub>, which is important for oxygen activation [78]. Upon UV light pre-treatment, no photo-generated holes and electrons are

produced (as  $\text{SiO}_2$  is an insulator) hence the lack of any improvement in activity. Additionally, the cubooctahedral shape of the Pt deposits on the  $\text{SiO}_2$  surface may favor adsorbed oxygen dissociation and activation compared to the hemispherical Pt deposits on  $\text{TiO}_2$  providing the elevated activity seen for  $\text{Pt}/\text{SiO}_2$ .

The mechanisms proposed for photocatalytic ROS formation and FA oxidation by  $\text{Pt}/\text{TiO}_2$ ,  $\text{Pt}/\text{CeO}_2$  and  $\text{Pt}/\text{SiO}_2$  are depicted in Fig. S12. For the  $\text{Pt}/\text{TiO}_2$  system (Fig. S12a), the following processes are thought to occur: (i) the reduction of molecular oxygen to adsorbed oxygen on the Pt and  $\text{TiO}_2$  surfaces by the photogenerated  $\text{TiO}_2$  conduction band electrons ( $e_{\text{CB}}^-$ ); and (ii) water oxidation by the photo-generated holes ( $h_{\text{VB}}^+$ ) contributing predominantly to hydroxyl radical formation (as well as other oxidizing species). These events are the primary redox processes controlling photocatalysis by  $\text{Pt}/\text{TiO}_2$  in an aqueous system. The mechanism proposed for the photocatalytic oxidation of FA by  $\text{Pt}/\text{CeO}_2$  is shown in Fig. S12b. Upon UV illumination, photo-excited electron-hole pairs are generated on the  $\text{CeO}_2$  surface. While the Pt loaded on the  $\text{CeO}_2$  surface is in an oxidized state (i.e.  $\text{Pt}^{2+}$  and  $\text{Pt}^{4+}$ ), it can still trap electrons from the  $\text{CeO}_2$  conduction band. However, a shorter charge carrier lifetime is expected as  $\text{Pt}_{\text{ox}}$  may also act as a recombination center for the photogenerated electrons and holes [21]. The oxygen vacancy states associated with  $\text{Ce}^{3+}$  can trap electrons as well, which can subsequently interact with adsorbed  $\text{O}_2$  to form  $\cdot\text{O}_2^-$  [74]. Holes on the  $\text{CeO}_2$  surface can be consumed by water molecules or hydroxyl groups to form  $\cdot\text{OH}$  and, similar to the  $\text{Pt}/\text{TiO}_2$ , the  $\cdot\text{O}_2^-$  and  $\cdot\text{OH}$  can then oxidise the FA. Owing to its powerful nucleophilicity, both radicals have the tendency to attack the positively charged carbon in formic acid to further generate  $\text{CO}_2$  and  $\text{H}_2\text{O}$  [79].

In the case of  $\text{Pt}/\text{SiO}_2$  (Fig. S12c), minimal photocatalysis is expected as  $\text{SiO}_2$  is an insulator. However, based on the ROS measurements, some  $\cdot\text{OH}$  and  $\cdot\text{O}_2^-$  were generated (Fig. 8). There exists the possibility of defects in the  $\text{SiO}_2$  structure which may trap electrons to produce a small amount of ROS upon UV illumination. The cubooctahedral shape of the Pt deposits, which possess a greater number of sharp edges/corners at the interface between the (111) and (200) crystals facets, may also facilitate the adsorption, dissociation and activation of oxygen and promote FA oxidation. It was reported that the predominant effects of adsorbed oxygen are to (i) facilitate the conversion of formic acid to formate [80] and (ii) increase the stability of the formate to attain maximum desorption of  $\text{CO}_2$  and  $\text{H}_2\text{O}$  [81].

#### 4. Conclusions

The findings presented here provide new understanding into the catalytic and photocatalytic oxidation of FA on different supports ( $\text{TiO}_2$ ,  $\text{CeO}_2$  and  $\text{SiO}_2$ ) with and without Pt deposits. Insights into the generation and subsequent role of key oxidizing species under different conditions were also established. Under dark catalytic conditions with and without UV light pre-treatment, surface active oxygen species ( $\text{PtO}_{\text{ads}}$  and  $\text{O}_{\text{ads}}^-$ ) were found to be the primary active species for the oxidation reaction while under photocatalytic conditions, hydroxyl ( $\cdot\text{OH}$ ) and superoxide anion ( $\cdot\text{O}_2^-$ ) radicals provided an additional contribution. The supports were crucial in defining the type and amount of oxidizing species in the presence and absence of illumination. Under dark conditions, properties of the Pt deposits, including shape, size, exposed facets and oxidation state (which were governed by the support and then further influenced by the UV pre-treatment step), were important contributors to the amount and type of oxidizing species. A semiconductor support in conjunction with metallic Pt deposits, as is present for the  $\text{Pt}/\text{TiO}_2$  system, is a prerequisite for light pre-treatment to provide any beneficial effect. Interestingly, the  $\text{Pt}/\text{SiO}_2$  catalyst demonstrated the highest level of surface active oxygen species and, in turn, the highest dark (i.e. no illumination) FA oxidation rate, although the insulating nature of the  $\text{SiO}_2$  support meant that there was little improvement in performance when exposed to UV light. The cubooctahedral shape of the Pt deposits on the  $\text{SiO}_2$  is thought to be a

major contributor to its elevated dark catalytic activity in this instance.

#### Acknowledgments

This work was supported by the Australian Research Council under The Laureate Fellowship Scheme – FL140100081. W.H. Saputera thanks the Indonesia Endowment Fund for Education (LPDP), Republic of Indonesia for financing his PhD scholarship. The authors would like to acknowledge the UNSW Mark Wainwright Analytical Centre for their assistance with XPS, TEM, ICP, and XRD measurements and analysis. The authors also acknowledge the use of facilities within the UoW Electron Microscopy Centre (Dr. David Mitchell and Dr. Gilberto Casillas-Garcia).

#### Appendix A. Supplementary data

Supplementary data associated with this article can be found, in the online version, at <http://dx.doi.org/10.1016/j.apcatb.2017.08.083>.

#### References

- [1] C. Zhang, H. He, K.-i. Tanaka, *Catal. Commun.* 6 (2005) 211–214.
- [2] C. Zhang, H. He, K.-i. Tanaka, *Appl. Catal. B* 65 (2006) 37–43.
- [3] C. Ma, D. Wang, W. Xue, B. Dou, H. Wang, Z. Hao, *Environ. Sci. Technol.* 45 (2011) 3628–3634.
- [4] C. Zhang, Y. Li, Y. Wang, H. He, *Environ. Sci. Technol.* 48 (2014) 5816–5822.
- [5] L. Ma, D. Wang, J. Li, B. Bai, L. Fu, Y. Li, *Appl. Catal. B* 148–149 (2014) 36–43.
- [6] G. Ertl, H. Knozinger, F. Schüth, J. Weitkamp, *Handbook of Heterogeneous Catalysis*, 2nd ed., Wiley-VCH, 2008.
- [7] J. Disdier, J.-M. Herrmann, P. Pichat, *J. Chem. Soc. Faraday Trans. Phys. Chem. Condensed Phases* 79 (1983) 651–660.
- [8] A.O.T. Patrocínio, J. Schneider, M.D. Franca, L.M. Santos, B.P. Caixeta, A.E.H. Machado, D.W. Bahnemann, *RSC Adv.* 5 (2015) 70536–70545.
- [9] F. Denny, J. Scott, K. Chiang, W.Y. Teoh, R. Amal, *J. Mol. Catal. A: Chem.* 263 (2007) 93–102.
- [10] J. Scott, W. Irawaty, G. Low, R. Amal, *Appl. Catal. B* 164 (2015) 10–17.
- [11] K. Kon, S.M.A. Hakim Siddiki, K.-i. Shimizu, *J. Catal.* 304 (2013) 63–71.
- [12] Y. Li, F. Zaera, *J. Catal.* 326 (2015) 116–126.
- [13] C.-K. Tsung, J.N. Kuhn, W. Huang, C. Aliaga, L.-I. Hung, G.A. Somorjai, P. Yang, *J. Am. Chem. Soc.* 131 (2009) 5816–5822.
- [14] C.M. Sánchez-Sánchez, J. Solla-Gullón, F.J. Vidal-Iglesias, A. Aldaz, V. Montiel, E. Herrero, *J. Am. Chem. Soc.* 132 (2010) 5622–5624.
- [15] S. Cao, J. Jiang, B. Zhu, J. Yu, *Phys. Chem. Chem. Phys.* 18 (2016) 19457–19463.
- [16] V. Grozovski, J. Solla-Gullón, V. Climent, E. Herrero, J.M. Feliz, *J. Phys. Chem. C* 114 (2010) 13802–13812.
- [17] Y. Xia, Y. Xiong, B. Lim, S.E. Skrabalak, *Angew. Chem. Int. Ed.* 48 (2009) 60–103.
- [18] C.J. Kliewer, C. Aliaga, M. Bieri, W. Huang, C.-K. Tsung, J.B. Wood, K. Komvopoulos, G.A. Somorjai, *J. Am. Chem. Soc.* 132 (2010) 13088–13095.
- [19] V. Komanicky, A. Menzel, H. You, *J. Phys. Chem. B* 109 (2005) 23550–23557.
- [20] N. An, W. Zhang, X. Yuan, B. Pan, G. Liu, M. Jia, W. Yan, W. Zhang, *Chem. Eng. J.* 215–216 (2013) 1–6.
- [21] J. Lee, W. Choi, *J. Phys. Chem. B* 109 (2005) 7399–7406.
- [22] W.Y. Teoh, L. Mäder, R. Amal, *J. Catal.* 251 (2007) 271–280.
- [23] T. Sano, N. Negishi, K. Uchino, J. Tanaka, S. Matsuzawa, K. Takeuchi, *J. Photochem. Photobiol. A: Chem.* 160 (2003) 93–98.
- [24] K. Kon, S.M.A. Hakim Siddiki, K.-i. Shimizu, *J. Catal.* 304 (2013) 63–71.
- [25] A. Alessi, S. Agnelli, G. Buscarino, Y. Pan, I.R. Mashkovtsev, A. Lund, M. Shiotani (Eds.), *Applications of EPR in Radiation Research*, Springer International Publishing, Cham, 2014, pp. 255–295.
- [26] M.W. Breiter, *Electrochim. Acta* 8 (1963) 447–456.
- [27] J.M.A. Harmsen, L. Jelemsky, P.J.M. Van Andel-Scheffer, B.F.M. Kuster, G.B. Marin, *Appl. Catal. A* 165 (1997) 499–509.
- [28] N. Akiya, P.E. Savage, *AIChE J.* 44 (1998) 405–415.
- [29] R. Tohmon, Y. Shimogaichi, Y. Tsuta, S. Munekuni, Y. Ohki, Y. Hama, K. Nagasawa, *Phys. Rev. B* 41 (1990) 7258–7260.
- [30] M. Stapelbroek, D.L. Griscom, E.J. Friebel, G.H. Sigel, *J. Non-Cryst. Solids* 32 (1979) 313–326.
- [31] G. Kovács, S. Fodor, A. Vulpoi, K. Schrantz, A. Dombi, K. Hernádi, V. Danciu, Z. Pap, L. Baia, *J. Catal.* 325 (2015) 156–167.
- [32] S. Bai, L. Wang, Z. Li, Y. Xiong, *Adv. Sci. 4* (2017) (1600216-n/a).
- [33] Y. Zhou, D.E. Doronkin, M. Chen, S. Wei, J.-D. Grunwaldt, *ACS Catal.* 6 (2016) 7799–7809.
- [34] M. Cao, Z. Tang, Q. Liu, Y. Xu, M. Chen, H. Lin, Y. Li, E. Gross, Q. Zhang, *Nano Lett.* 16 (2016) 5298–5302.
- [35] V.R. Stamenovic, B.S. Mun, M. Arenz, K.J.J. Mayrhofer, C.A. Lucas, G. Wang, P.N. Ross, N.M. Markovic, *Nat. Mater.* 6 (2007) 241–247.
- [36] M.J. Lundwall, S.M. McClure, X. Wang, Z.-j. Wang, M.-s. Chen, D.W. Goodman, *J. Phys. Chem. C* 116 (2012) 18155–18159.
- [37] S.M. Davis, F. Zaera, G.A. Somorjai, *J. Am. Chem. Soc.* 104 (1982) 7453–7461.

[38] W.-K. Wang, J.-J. Chen, W.-W. Li, D.-N. Pei, X. Zhang, H.-Q. Yu, *ACS Appl. Mater. Interfaces* 7 (2015) 20349–20359.

[39] C.L. Muhich, Y. Zhou, A.M. Holder, A.W. Weimer, C.B. Musgrave, *J. Phys. Chem. C* 116 (2012) 10138–10149.

[40] W.H. Saputera, J. Scott, N. Ganda, G.K.C. Low, R. Amal, *Catal. Sci. Technol.* 6 (2016) 6679–6687.

[41] W.H. Saputera, J. Scott, H. Tahini, G.K.C. Low, X. Tan, S. Smith, D.-W. Wang, R. Amal, *ACS Catal.* 7 (2017) 3644–3653.

[42] M.A.L. Rocha, G. Del Ángel, G. Torres-Torres, A. Cervantes, A. Vázquez, A. Arrieta, J.N. Beltramini, *Catal. Today* 250 (2015) 145–154.

[43] Evonik, AEROXIDE®, AERODISP® AND AEROPERL® Titanium Dioxide as Photocatalyst, Evonik, Germany, 2015, 4–11.

[44] R.W. Matthews, M. Abdullah, G.K.C. Low, *Anal. Chim. Acta* 233 (1990) 171–179.

[45] H. Czili, A. Horváth, *Appl. Catal. B* 81 (2008) 295–302.

[46] H. Goto, Y. Hanada, T. Ohno, M. Matsumura, *J. Catal.* 225 (2004) 223–229.

[47] S. Alayoglu, K. An, G. Melaet, S. Chen, F. Bernardi, L.W. Wang, A.E. Lindeman, N. Musselwhite, J. Guo, Z. Liu, M.A. Marcus, G.A. Somorjai, *J. Phys. Chem. C* 117 (2013) 26608–26616.

[48] Y. Zhu, D. Liu, M. Meng, *Chem. Commun.* 50 (2014) 6049–6051.

[49] Y. Inaki, H. Yoshida, T. Yoshida, T. Hattori, *J. Phys. Chem. B* 106 (2002) 9098–9106.

[50] L. Yuliati, M. Tsubota, A. Satsuma, H. Itoh, H. Yoshida, *J. Catal.* 238 (2006) 214–220.

[51] M.S. Spencer, *J. Catal.* 93 (1985) 216–223.

[52] F.B. Li, X.Z. Li, *Chemosphere* 48 (2002) 1103–1111.

[53] S. Kim, S.-J. Hwang, W. Choi, *J. Phys. Chem. B* 109 (2005) 24260–24267.

[54] B. Ohtani, O.O. Prieto-Mahaney, D. Li, R. Abe, *J. Photochem. Photobiol. A: Chem.* 216 (2010) 179–182.

[55] L. Zhao, N. Li, A. Langner, M. Steinhart, T.Y. Tan, E. Pippel, H. Hofmeister, K.N. Tu, U. Gösele, *Adv. Funct. Mater.* 17 (2007) 1952–1957.

[56] I. Onal, J.B. Butt, *J. Chem. Soc. Faraday Trans. Phys. Chem. Condensed Phases* 78 (1982) 1887–1898.

[57] Y. Borodko, P. Ercius, V. Pushkarev, C. Thompson, G. Somorjai, *J. Phys. Chem. Lett.* 3 (2012) 236–241.

[58] C. Hodnik, G. Baldizzone, S. Polymeros, J.-P. Geiger, S. Grote, A. Cherevko, A. Mingers, K.J.J. Zeradjanin, *Nat. Commun.* 7 (2016) 13164.

[59] S. Hwang, M.C. Lee, W. Choi, *Appl. Catal. B* 46 (2003) 49–63.

[60] S. Sakthivel, M.V. Shankar, M. Palanichamy, B. Arabindoo, D.W. Bahnemann, V. Murugesan, *Water Res.* 38 (2004) 3001–3008.

[61] W.Y. Teoh, L. Mädler, D. Beydoun, S.E. Pratsinis, R. Amal, *Chem. Eng. Sci.* 60 (2005) 5852–5861.

[62] W.-N. Wang, W.-J. An, B. Ramalingam, S. Mukherjee, D.M. Niedzwiedzki, S. Gangopadhyay, P. Biswas, *J. Am. Chem. Soc.* 134 (2012) 11276–11281.

[63] C.H. Choi, M. Kim, H.C. Kwon, S.J. Cho, S. Yun, H.-T. Kim, K.J.J. Mayrhofer, H. Kim, M. Choi, *Nat. Commun.* 7 (2016) 10922.

[64] N. Tian, Z.-Y. Zhou, S.-G. Sun, Y. Ding, Z.L. Wang, *Science* 316 (2007) 732–735.

[65] A.C. Ngandjou, C. Mottet, J. Puibasset, *J. Phys. Chem. C* 120 (2016) 8323–8332.

[66] K. Kinoshita, *J. Electrochem. Soc.* 137 (1990) 845–848.

[67] K. Harrison, L.B. Hazell, *Surf. Interface Anal.* 18 (1992) 368–376.

[68] W. Lin, A.A. Herzing, C.J. Kiely, I.E. Wachs, *J. Phys. Chem. C* 112 (2008) 5942–5951.

[69] Y. Gao, W. Wang, S. Chang, W. Huang, *ChemCatChem* 5 (2013) 3610–3620.

[70] S.A. Ansari, M.M. Khan, M.O. Ansari, S. Kalathil, J. Lee, M.H. Cho, *RSC Adv.* 4 (2014) 16782–16791.

[71] S. Scirè, S. Minicò, C. Crisafulli, C. Satriano, A. Pistone, *Appl. Catal. B* 40 (2003) 43–49.

[72] Y. Bai, W. Li, C. Liu, Z. Yang, X. Feng, X. Lu, K.-Y. Chan, *J. Mater. Chem.* 19 (2009) 7055–7061.

[73] G.-Q. Gao, L. Lin, C.-M. Fan, Q. Zhu, R.-X. Wang, A.-W. Xu, *J. Mater. Chem. A* 1 (2013) 12206–12212.

[74] B. Choudhury, P. Chetri, A. Choudhury, *RSC Adv.* 4 (2014) 4663–4671.

[75] R.B. Getman, Y. Xu, W.F. Schneider, *J. Phys. Chem. C* 112 (2008) 9559–9572.

[76] M. Wakisaka, H. Suzuki, S. Mitsui, H. Uchida, M. Watanabe, *Langmuir* 25 (2009) 1897–1900.

[77] T. Li, P.B. Balbuena, *J. Phys. Chem. B* 105 (2001) 9943–9952.

[78] C.S. Ewing, G. Veser, J.J. McCarthy, J.K. Johnson, D.S. Lambrecht, *J. Phys. Chem. C* 119 (2015) 19934–19940.

[79] M. Hayyan, M.A. Hashim, I.M. AlNashef, *Chem. Rev.* 116 (2016) 3029–3085.

[80] N.R. Avery, *Appl. Surf. Sci.* 11 (1982) 774–783.

[81] M.R. Columbia, P.A. Thiel, *Chem. Phys. Lett.* 220 (1994) 167–171.